Supplement of Atmos. Chem. Phys., 24, 7421–7446, 2024
https://doi.org/10.5194/acp-24-7421-2024-supplement

Supplement of

Modeling impacts of dust mineralogy on fast climate response

Qianqian Song et al.

Correspondence to: Qianqian Song (qs7080@princeton.edu)

S1. Optical Properties of clay minerals

Three clay minerals are considered in this study: illite, kaolinite, and smectite. These three clay minerals have a similar layered structure and have the same role in carrying iron oxides to remote regions through internally mixing with iron oxides. The similarities among the three clay minerals lead us to consider treating them as a single mineral when calculating their optical properties in their interaction with radiation. In the calculations of optical properties for the GFDL AM4.0 model, they are considered as an external mixture when treated as three separate minerals, and as an internal mixture when treated as a single mineral. Therefore, this section aims to investigate the similarities in the optical properties between their internal and external mixtures.

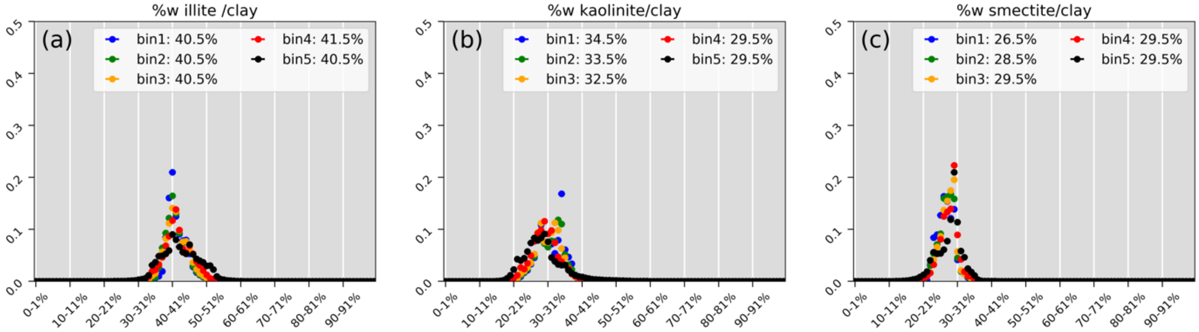

Figure S1. Histogram of mass fraction of (a) illite, (b) kaolinite and (c) smectite with respect to total clay minerals (i.e., the sum of the three minerals) for five size bins respectively. The mass fraction data is modeled all over the world for 19 years (2001-2019). The legend indicates the peak mass fraction for each size bin.

The mixing ratio of the three clay minerals is required for calculating the optical properties of their internal and external mixtures. Figure S1 displays the histogram of mass fraction ($\%w$) of illite, kaolinite, and smectite with respect to the total clay minerals based on 19 years of AM4.0 simulations. It suggests that in the atmosphere, illite, kaolinite and smectite generally account for 40%, 30% and 30% of the total clay minerals in terms of mass, respectively. Therefore, we assume the mass (or volume) fraction of illite, kaolinite and smectite in their mixtures is 40%,30% and 30%. The optical properties of their internal mixtures are calculated by using three mixing rules: VOL-mixing, MG-mixing, and BG-mixing.

Figure S2 shows the optical properties of the three clay minerals and their internal and external mixtures. The optical properties of the three individual clay minerals are similar in mass extinction coefficient (ε) and asymmetry parameter (g), but distinct in SSA. In the visible spectrum, kaolinite exhibits the most scattering clay mineral, smectite shows the most absorption, while illite falls in the middle. Regarding their internal mixtures of the clay minerals with mass fraction of 40% illite, 30% kaolinite and 30% smectite (referred to as clay433 hereafter), the three mixing rules lead to almost identical optical properties. Most importantly, the optical properties of their internal mixtures and external mixtures are very similar. Therefore, the results suggest that we could use a single mineral species (i.e., clay433) to represent all three clay minerals in their interaction with radiation to reduce computational cost.

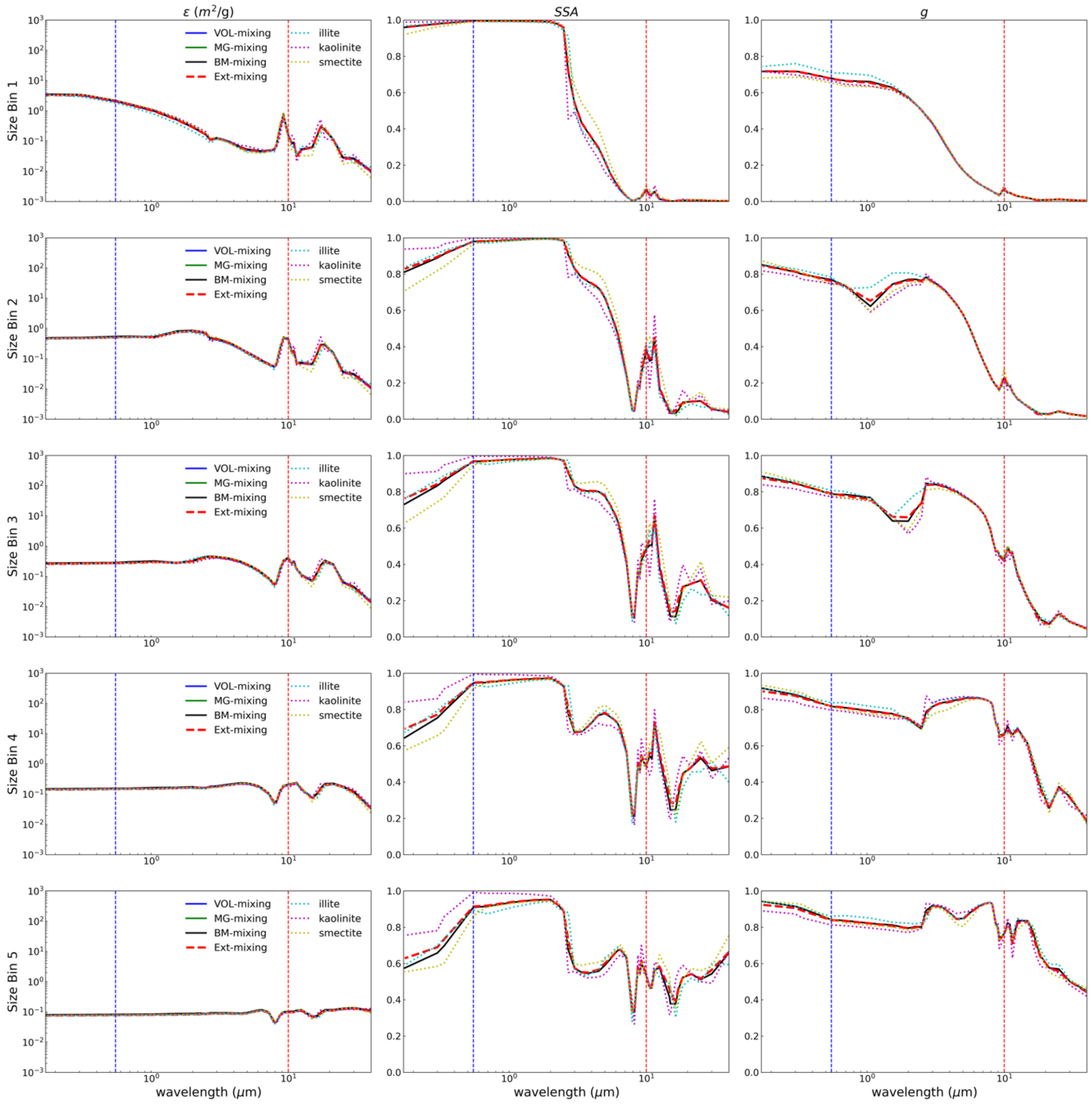

Figure S2. Mass extinction coefficient (ε), single scattering albedo (SSA), and asymmetry parameter (*g*) for three clay minerals (i.e., illite, kaolinite, and smectite), their internal mixtures (i.e., VOL-mixing, MG-mixing, and BM-mixing), and their external mixtures (i.e., Ext-mixing). The mass (or volume) fraction of illite, kaolinite and smectite in their mixtures is assumed to be 40%,30% and 30%, respectively. The vertical blue and red dashed lines highlight wavelength at 550nm and 10μm.

S2. Dust Properties

Table S1. Annual mean (2001-2019) dust emission, atmospheric load, and deposition global budgets (Tg). Lifetime (days). GA-2023 is the results from Gonçalves Ageitos et al., 2023 based on C1999 soil map. Clay: illite, kaolinite, and smectite.

	C1999	quartz	calcite	feldspar	gypsum	hematite	clay
Emission (Tg/yr)	VOL	1173.5	189.3	446.8	45.7	48.6	1249.7
	MG	1144.9	184.6	439.2	44.7	47.4	1221.7
	BM	1147.9	185.7	437.7	44.8	47.6	1223.5
	GA-2023	1359.6	181.8	451.9	47.2	56	1386.0
Load (Tg)	VOL	6.9	1.2	2.7	0.3	0.3	10.2
	MG	6.7	1.2	2.7	0.3	0.3	10.0
	BM	6.7	1.2	2.6	0.3	0.3	9.9
	GA-2023	9.8	1.3	3.3	0.4	0.5	13.2
Dry deposition (Tg/yr)	VOL	905.6	141.5	344.5	33.1	35.3	859.8
	MG	886.4	138.5	339.5	32.5	34.6	843.8
	BM	887.5	138.9	338.1	32.4	34.7	843.9
	GA-2023	820.1	109.1	273.3	27.1	31.4	760.4
Wet deposition (Tg/yr)	VOL	267.6	47.7	102.2	12.6	12.8	389.7
	MG	258.2	46.0	99.6	12.2	12.8	377.5
	BM	260.2	46.8	99.5	12.3	12.8	379.3
	GA-2023	511.2	68.5	169.5	18.9	23.2	582.2
Total deposition (Tg/yr)	VOL	1173.3	189.2	446.7	45.6	48.1	1249.5
	MG	1144.6	184.5	439.1	44.7	47.3	1221.3
	BM	1147.8	185.7	437.7	44.8	47.5	1223.2
	GA-2023	1331.3	177.6	442.9	46.0	54.6	1342.5
Lifetime (days)	VOL	2.1	2.4	2.2	2.6	2.5	3.0
	MG	2.1	2.4	2.2	2.6	2.5	3.0
	BM	2.1	2.4	2.2	2.6	2.5	3.0
	GA-2023	2.7	2.7	2.8	3.0	3.2	3.6

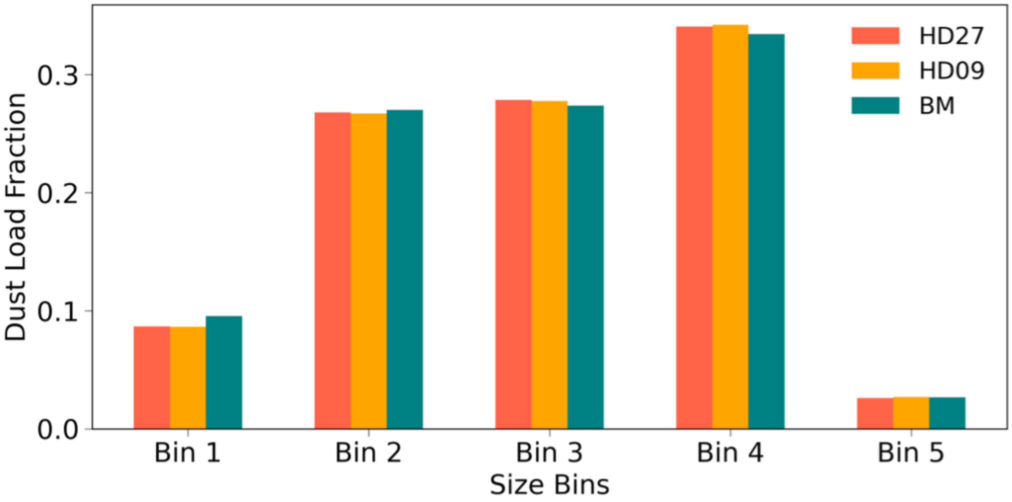

Figure S3. The dust load fraction in each size bin is analyzed for two homogeneous dust experiments (e.g., HD27 and HD09) and a mineral-resolved experiment (e.g., BM). These fractions are calculated based on the 19-year (2001-2019) global dust load. The size diameter range for each size bin is 0.2 - 2 μm for bin1, 2 - 3.6 μm for bin2, 3.6 - 6 μm for bin3, 6 - 12 μm for bin4, 12 - 20 μm for bin5.

S3. Evaluation Metrics

The evaluation of modeled dust SSA against observation-based results utilizes two evaluation metrics: the normalized mean bias (nMB) and normalized root mean square error ($nRMSE$).

$$nMB = \frac{\sum_i (M_i - O_i)}{\sum_i O_i} \times 100\%$$

$$nRMSE = \frac{\sqrt{\frac{1}{N}\sum_i (M_i - O_i)^2}}{\frac{1}{N}\sum_i O_i} \times 100\%$$

Where, M_i represents the modelled value at the observation location and time, O_i represents the corresponding observed value, and N the number of observations considered.

S4. The Sensitivity of Dust SSA to Dust Size

In Figure 5 (a) in the main text, the two homogeneous dust experiments (i.e., HD27 and HD09) show different regional variabilities, which is indicated by their standard deviation (σ). The more absorptive HD27 dust ($\sigma = 0.006$) shows higher regional variability than the less absorptive HD09 dust ($\sigma = 0.004$). Both the HD27 and HD09 experiments consider dust composition to be uniform without spatial and temporal variations, while HD27 contains more hematite than HD09 as described in Table 2 in the main text. Therefore, the regional variation of SSA in both experiments is solely attributed to the regional difference in dust size.

Here, we conducted a simple test to investigate the impact of dust size on dust SSA for the two homogeneous dust RIs, namely HD27 and HD09. We utilized five dust particle size distributions (PSDs) that represented a range from fine to coarse dust. Specifically, the i^{th} PSD has mass fraction of 0.6 in the i^{th} size bin, while the rest size bins have a mass fraction of 0.1, as illustrated in Figure S4a. The 1st PSD is the finest and the 5th PSD is the coarsest PSD in the test.

The dust SSA in Figure S4b is calculated using the five PSDs for both HD27 and HD09 dust RIs. For a given dust RI, coarser dust is more absorptive than finer dust (Figure S4b). This observation aligns with well-established findings supported by previous studies (Ryder et al., 2018). HD27 dust is always more absorptive than HD09 dust for the same PSD due to its higher iron oxide content. Importantly, the results highlight that the SSA span for HD27 dust (0.064) induced by the PSD is larger than that for HD09 dust (0.041). This suggests that the variation in SSA due to the dust particle size is more pronounced for more absorptive HD27 dust compared to HD09 dust. This finding is supported by Figure S5, where we eliminate the effect from dust RI on SSA by grouping our experiments into two categories: homogeneous dust (HD27 and HD09) and mineral-resolved dust (VOL, MG, and BM). By doing this, within each group, the SSA spatial variation is solely attributed to the spatial variation of dust size. It is evident that more absorptive dust (i.e., lower mSSA) exhibits higher SSA variation (i.e., higher σ) when the effect from dust RI on SSA is eliminated.

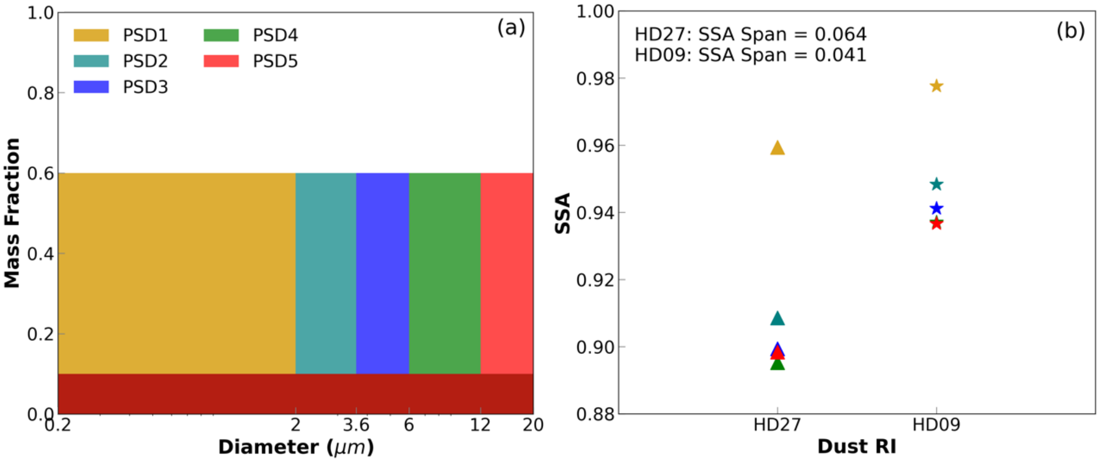

Figure S4. (a) illustrates five dust particle size distributions (PSDs) representing a range from fine to coarse dust. (b) displays dust SSA on the y-axis for two different dust RIs, HD27 (triangles) and HD09 (stars), indicated on the x-axis. The five colors represent the five PSDs, as shown in (a).

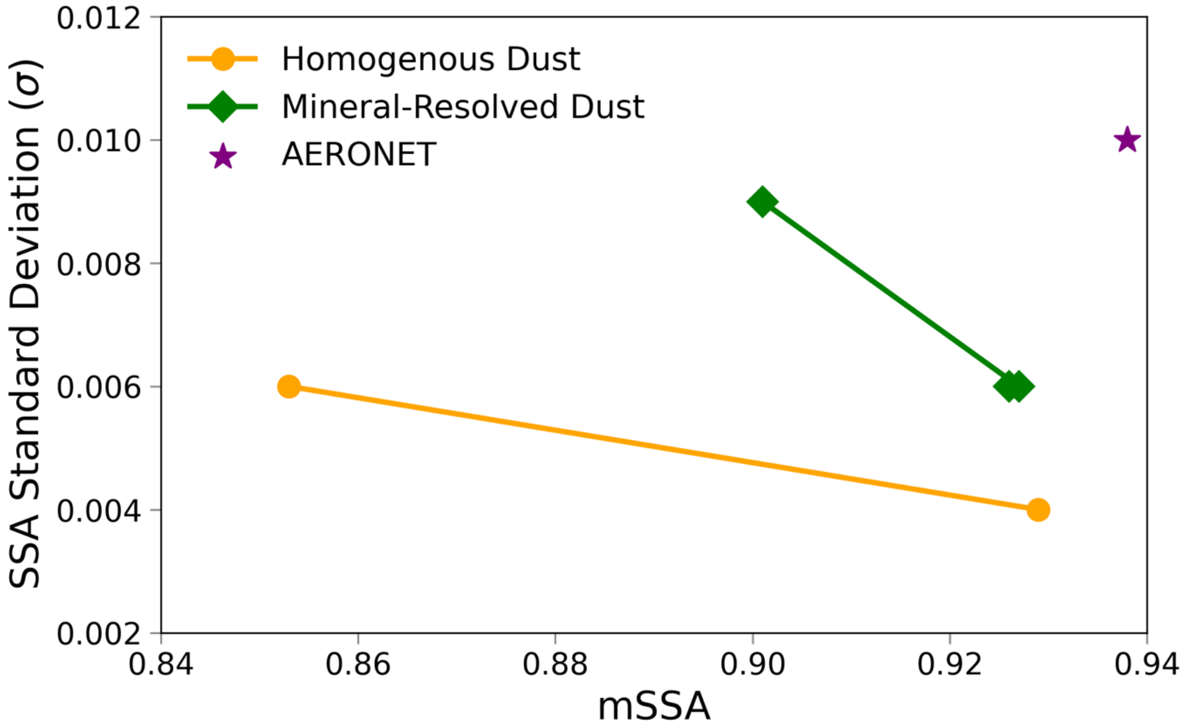

Figure S5. The standard deviation (σ) of SSA versus the mean SSA (mSSA) at AERONET sites shown in Figure 5 in the main text. The orange line is for homogeneous dust HD27 and HD09. The green line is for mineral-resolved dust VOL, MG, and BM. The purple star represents AERONET retrievals.

S5. Impacts of resolving dust mineralogy on clear-sky radiative fluxes on global scale

Figure S6-S13 show the clear-sky radiative flux anomalies at TOA and surface (SFC) induced by resolving dust mineralogy over the global scale (60°S-60°N, polar regions are not included). We calculate the domain averaged anomalies for the North Africa and Asia regions, which cover the most of the Dust Belt region (Prospero et al., 2002). We consider two seasons: JJA, when the Sahara dust sources are the most active, and MAM, when the Asian dust sources are the most active.

Figure S6, S8, S10 and S12 display the clear-sky radiative flux anomalies induced by resolving dust mineralogy relative to HD27 control run. The 1st row of the figures shows the clear-sky flux from HD27 control run, the 2nd row of the figures shows the flux anomalies. The domain averaged flux for the 1st row and flux anomalies for the 2nd row of two regions: the Sahara and Sahel, are shown in parentheses within the title of each figure. We found that, generally there are more statistically significant anomalies (i.e., dotted area) over the North Africa than Asia, and the absolute values of anomalies is generally greater over the North Africa than Asia. Therefore, our study focuses on the North Africa and JJA to investigate the impacts of resolving dust mineralogy on clear-sky radiative fluxes.

Figure S7, S9, S11 and S13 display the clear-sky radiative flux anomalies induced by resolving dust mineralogy relative to HD09 control run. Compared to HD27, we see much less significant anomalies for HD09 in both JJA and MAM over the global scale. This suggests that, in the case of GFDL AM4.0 model, resolving dust mineralogy induce a weak impact on clear-sky fluxes at TOA and SFC relative to HD09. Caution should be taken before generalizing, as specific uncertainties of our model, such as a continuous source function blurring spatial heterogeneity between sources, large uncertainty in soil texture and mineralogy, and numerical diffusion, may not exist in other models.

S5.1. Clear-sky radiative fluxes anomalies at TOA

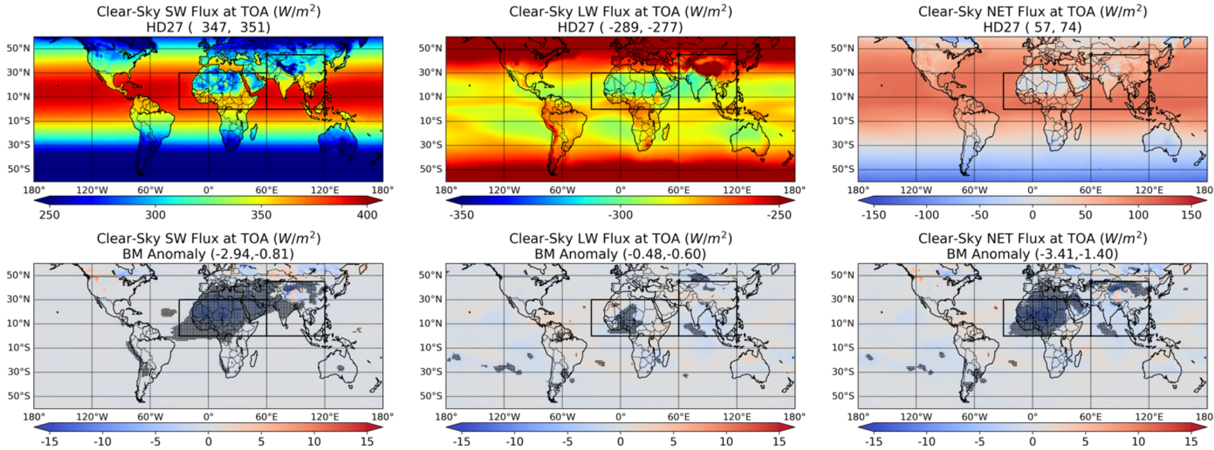
Clear-Sky SW Flux at TOA (W/m^2) HD27 (347, 351)

Clear-Sky LW Flux at TOA (W/m^2) HD27 (-289, -277)

Clear-Sky NET Flux at TOA (W/m^2) HD27 (57, 74)

Clear-Sky SW Flux at TOA (W/m^2) BM Anomaly (-2.94,-0.81)

Clear-Sky LW Flux at TOA (W/m^2) BM Anomaly (-0.48,-0.60)

Clear-Sky NET Flux at TOA (W/m^2) BM Anomaly (-3.41,-1.40)

Figure S6. HD27-MAM-TOA: 19-year (2001-2019) March-April-May (MAM) clear-sky radiative fluxes at TOA for the HD27 control run and their anomalies resulting from resolving mineral composition, based upon the Bruggeman mixing rule. The dotted area denotes anomalies that are statistically significant. The two values in parentheses within the title of each figure are domain averaged values for the North Africa and the Asia region.

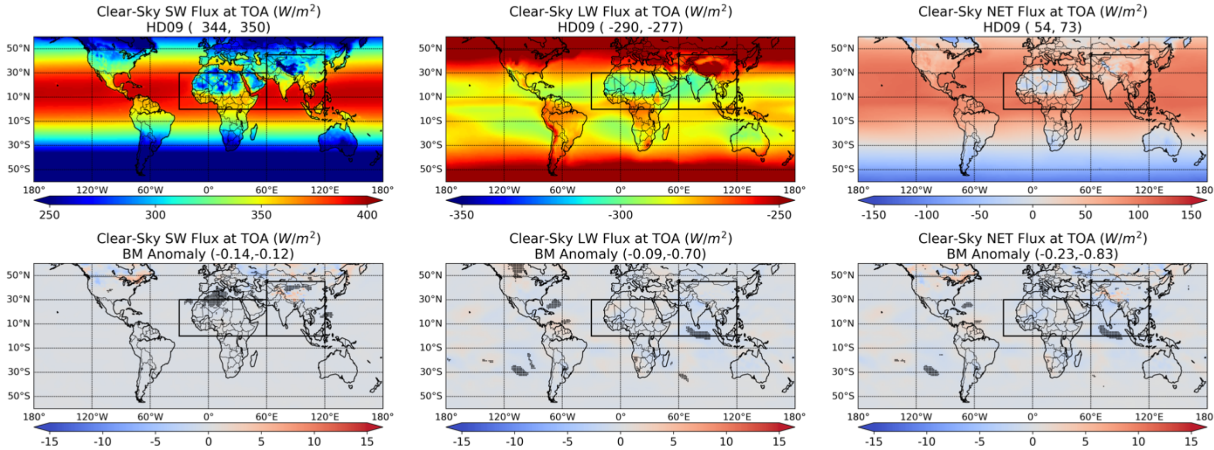
Clear-Sky SW Flux at TOA (W/m^2) HD09 (344, 350)

Clear-Sky LW Flux at TOA (W/m^2) HD09 (-290, -277)

Clear-Sky NET Flux at TOA (W/m^2) HD09 (54, 73)

Clear-Sky SW Flux at TOA (W/m^2) BM Anomaly (-0.14,-0.12)

Clear-Sky LW Flux at TOA (W/m^2) BM Anomaly (-0.09,-0.70)

Clear-Sky NET Flux at TOA (W/m^2) BM Anomaly (-0.23,-0.83)

Figure S7. HD09-MAM-TOA: The same as Figure S6, but with respect to HD09 control run.

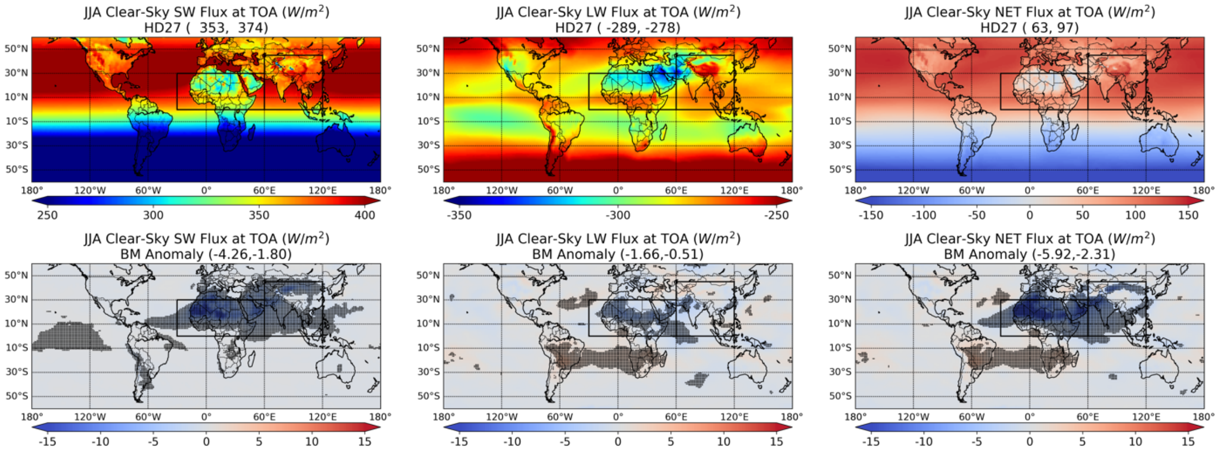
JJA Clear-Sky SW Flux at TOA (W/m^2) HD27 (353, 374)

JJA Clear-Sky LW Flux at TOA (W/m^2) HD27 (-289, -278)

JJA Clear-Sky NET Flux at TOA (W/m^2) HD27 (63, 97)

JJA Clear-Sky SW Flux at TOA (W/m^2) BM Anomaly (-4.26,-1.80)

JJA Clear-Sky LW Flux at TOA (W/m^2) BM Anomaly (-1.66,-0.51)

JJA Clear-Sky NET Flux at TOA (W/m^2) BM Anomaly (-5.92,-2.31)

Figure S8. HD27-JJA-TOA: The same as Figure S6, but for June-July-August (JJA)

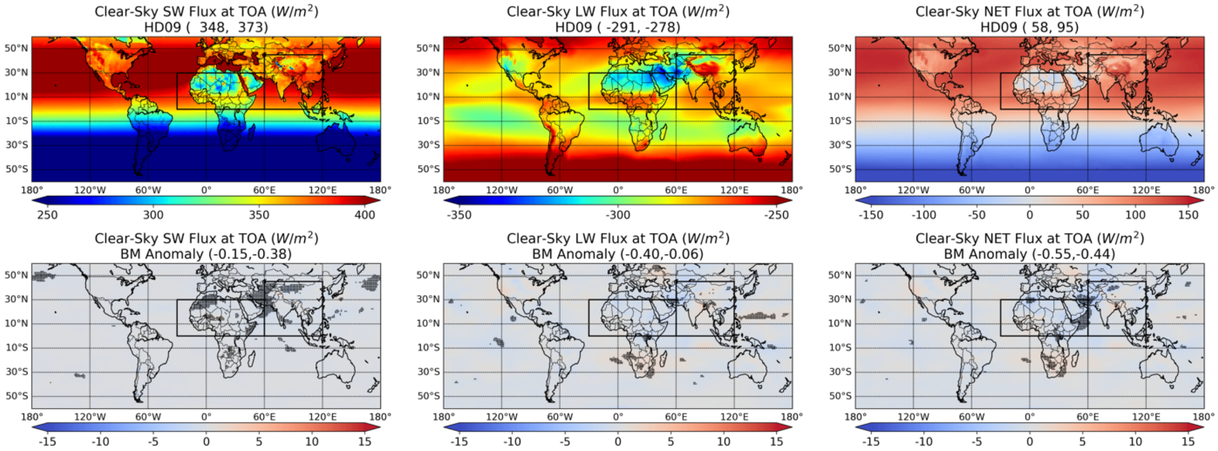
Clear-Sky SW Flux at TOA (W/m^2) HD09 (348, 373)

Clear-Sky LW Flux at TOA (W/m^2) HD09 (-291, -278)

Clear-Sky NET Flux at TOA (W/m^2) HD09 (58, 95)

Clear-Sky SW Flux at TOA (W/m^2) BM Anomaly (-0.15,-0.38)

Clear-Sky LW Flux at TOA (W/m^2) BM Anomaly (-0.40,-0.06)

Clear-Sky NET Flux at TOA (W/m^2) BM Anomaly (-0.55,-0.44)

Figure S9. HD09-JJA-TOA: The same as Figure S8, but with respect to HD09.

S5.2. Clear-sky radiative fluxes anomalies at Surface (SFC)

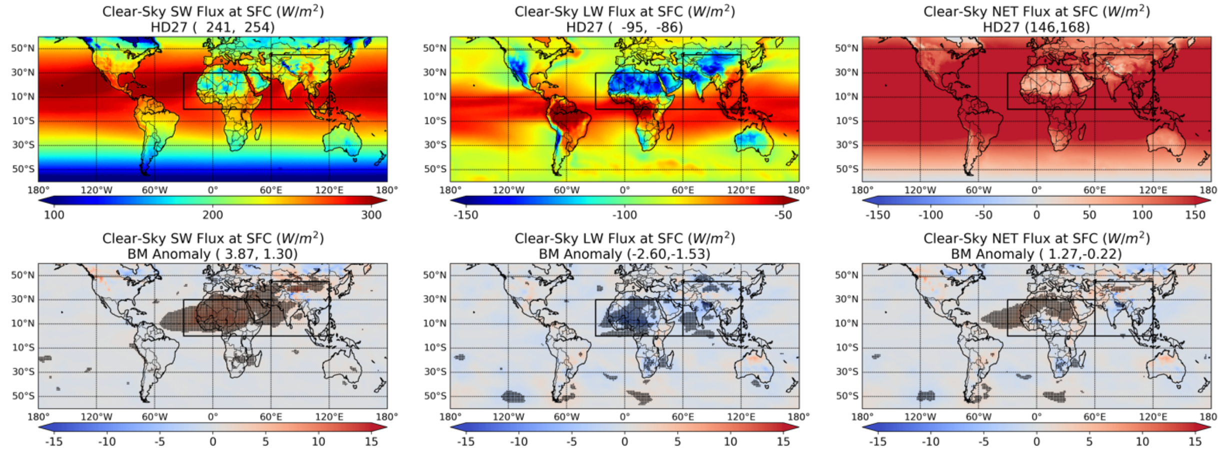

Figure S10. HD27-MAM-SFC: 19-year (2001-2019) March-April-May (MAM) clear-sky radiative fluxes at SFC for the HD27 control run and their anomalies resulting from resolving mineral composition, based upon the Bruggeman mixing rule. The dotted area denotes anomalies that are statistically significant. The two values in the parenthesis are domain averaged values for the North Africa and the Asia region.

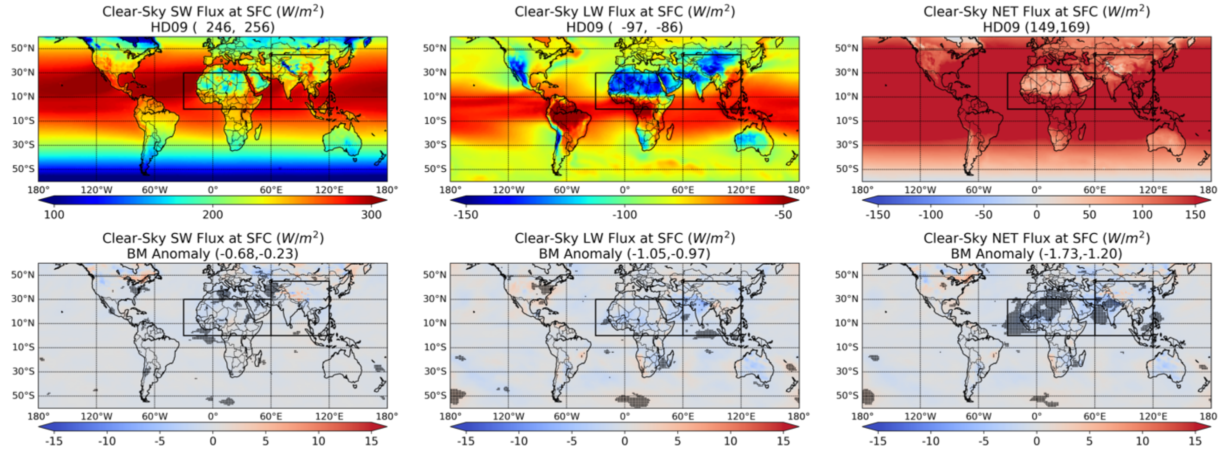

Figure S11. HD09-MAM-SFC: The same as Figure S10, but with respect to HD09.

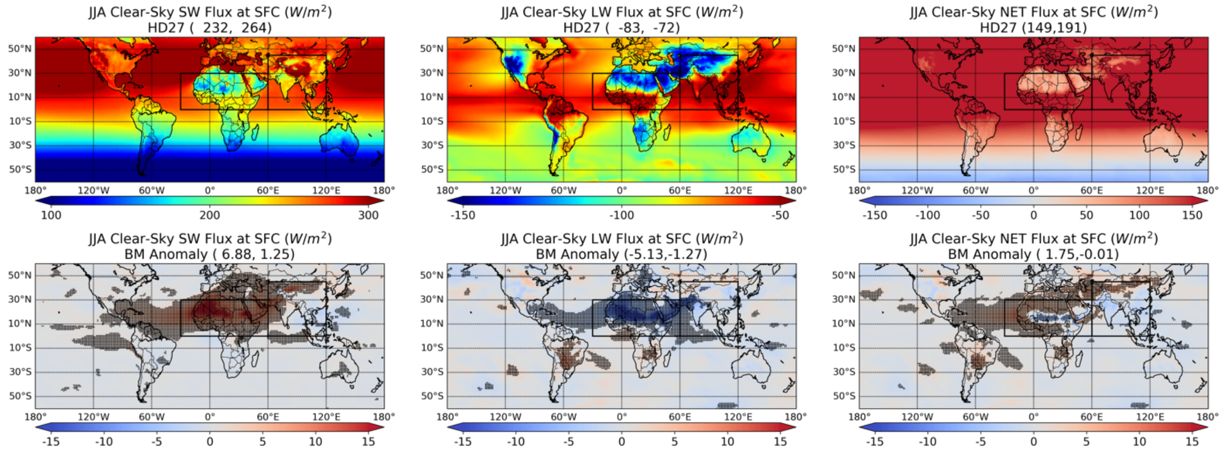

Figure S12. HD27-JJA-SFC: the same as Figure S10, but for JJA.

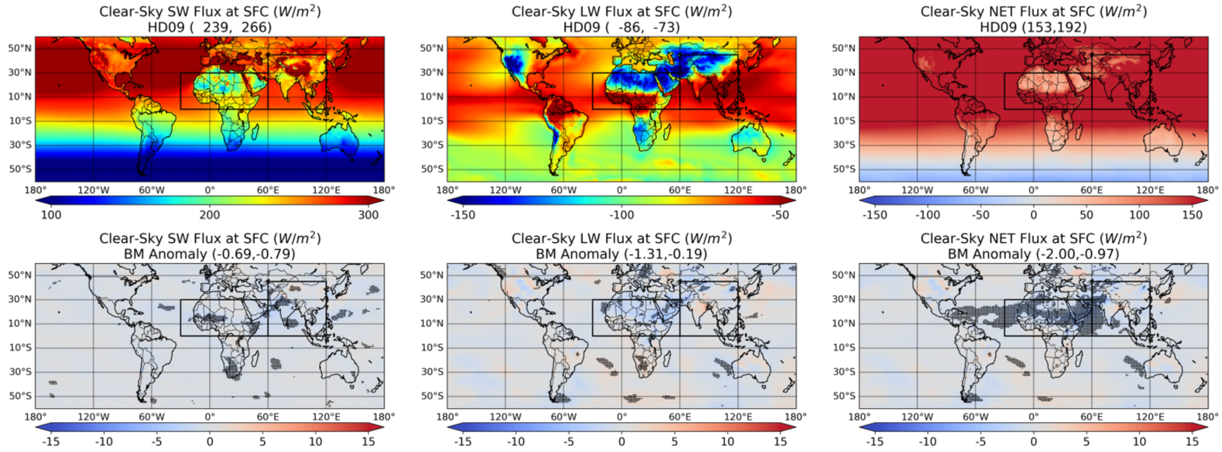

Figure S13. HD09-JJA-SFC: the same as Figure S12, but with respect to HD09.

S6. Potential in reducing mineral tracers

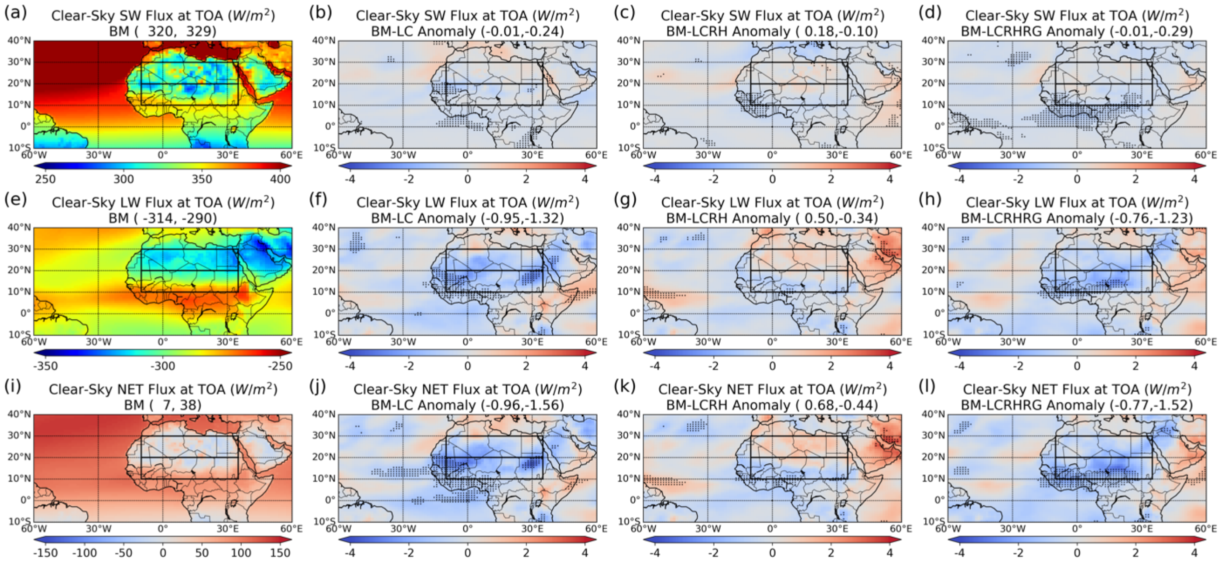
(a) Clear-Sky SW Flux at TOA (W/m^2) BM (320, 329)
(b) Clear-Sky SW Flux at TOA (W/m^2) BM-LC Anomaly (-0.01,-0.24)
(c) Clear-Sky SW Flux at TOA (W/m^2) BM-LCRH Anomaly (0.18,-0.10)
(d) Clear-Sky SW Flux at TOA (W/m^2) BM-LCRHRG Anomaly (-0.01,-0.29)
(e) Clear-Sky LW Flux at TOA (W/m^2) BM (-314, -290)
(f) Clear-Sky LW Flux at TOA (W/m^2) BM-LC Anomaly (-0.95,-1.32)
(g) Clear-Sky LW Flux at TOA (W/m^2) BM-LCRH Anomaly (0.50,-0.34)
(h) Clear-Sky LW Flux at TOA (W/m^2) BM-LCRHRG Anomaly (-0.76,-1.23)
(i) Clear-Sky NET Flux at TOA (W/m^2) BM (7, 38)
(j) Clear-Sky NET Flux at TOA (W/m^2) BM-LC Anomaly (-0.96,-1.56)
(k) Clear-Sky NET Flux at TOA (W/m^2) BM-LCRH Anomaly (0.68,-0.44)
(l) Clear-Sky NET Flux at TOA (W/m^2) BM-LCRHRG Anomaly (-0.77,-1.52)

Figure S14. Seasonal mean JJA climatology (2001-2019) clear-sky SW (1st row), LW (2nd row) and Net (3rd row) radiative flux at TOA for the reference experiment BM (1st column) and their anomalies resulting from reducing mineral tracers in BM-LC (2nd column), BM-LCRH (3rd column) and BM-LCRHRG (4th column). Downward flux is defined as positive. The dotted area denotes anomalies that are statistically significant. The two values in parentheses within the title of each figure are domain average for the Sahara and Sahel regions.

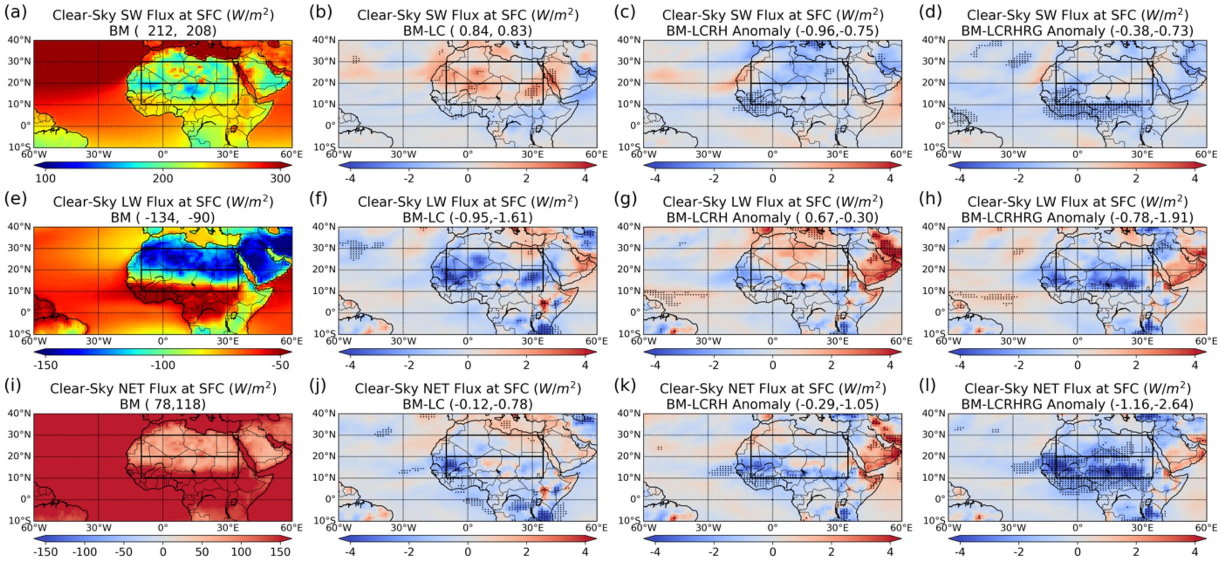
(a) Clear-Sky SW Flux at SFC (W/m^2) BM (212, 208)
(b) Clear-Sky SW Flux at SFC (W/m^2) BM-LC (0.84, 0.83)
(c) Clear-Sky SW Flux at SFC (W/m^2) BM-LCRH Anomaly (-0.96,-0.75)
(d) Clear-Sky SW Flux at SFC (W/m^2) BM-LCRHRG Anomaly (-0.38,-0.73)
(e) Clear-Sky LW Flux at SFC (W/m^2) BM (-134, -90)
(f) Clear-Sky LW Flux at SFC (W/m^2) BM-LC (-0.95,-1.61)
(g) Clear-Sky LW Flux at SFC (W/m^2) BM-LCRH Anomaly (0.67,-0.30)
(h) Clear-Sky LW Flux at SFC (W/m^2) BM-LCRHRG Anomaly (-0.78,-1.91)
(i) Clear-Sky NET Flux at SFC (W/m^2) BM (78,118)
(j) Clear-Sky NET Flux at SFC (W/m^2) BM-LC (-0.12,-0.78)
(k) Clear-Sky NET Flux at SFC (W/m^2) BM-LCRH Anomaly (-0.29,-1.05)
(l) Clear-Sky NET Flux at SFC (W/m^2) BM-LCRHRG Anomaly (-1.16,-2.64)

Figure S15. As in Figure S14, but for the surface.

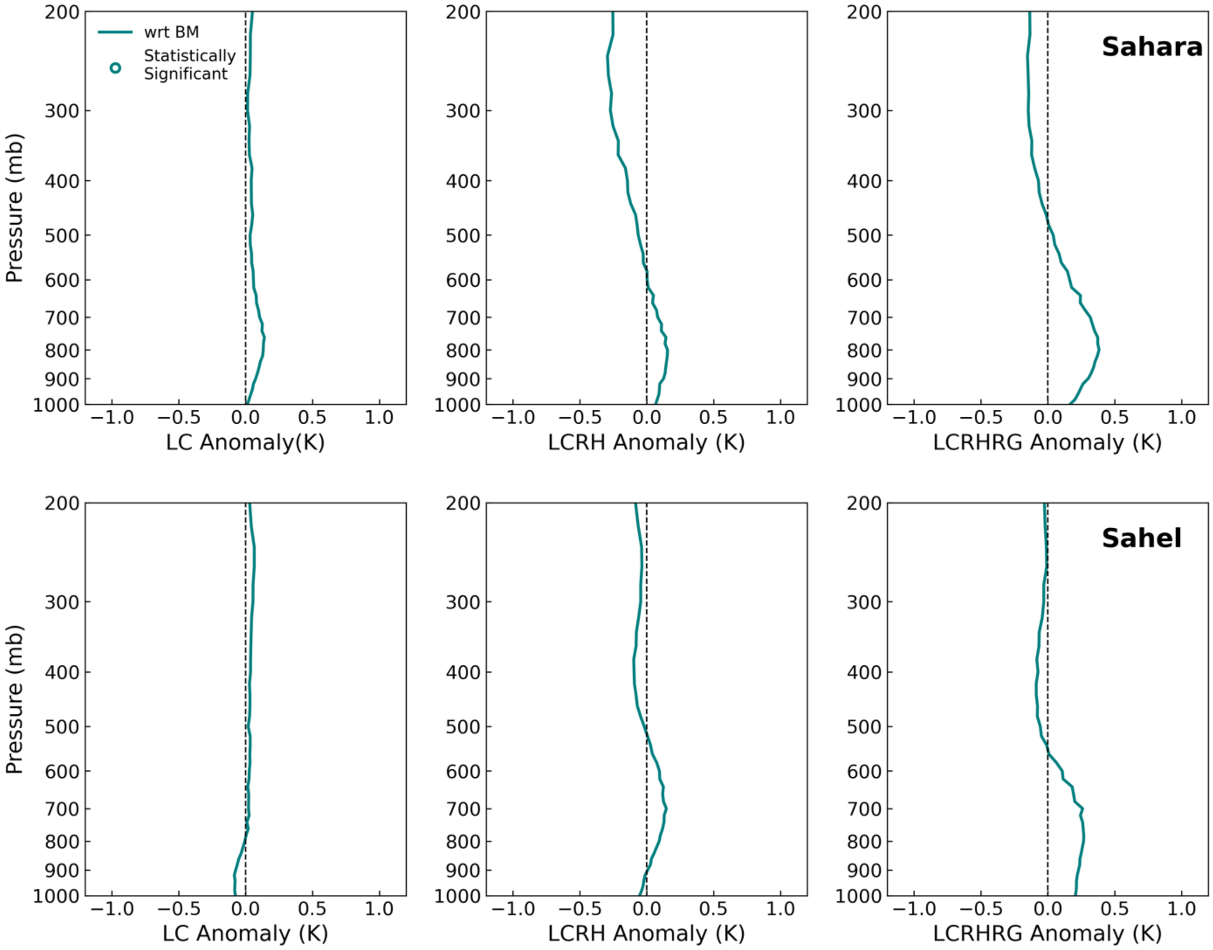

Figure S16. Temperature anomaly induced by reducing mineral tracers in BM for Sahara (1st row) and Sahel (2nd row) regions relative to the BM experiment. Similar to Figure 10 in the main text, circles represent statistically significant temperature anomaly (p-value < 0.05). No circles in the figure indicates no statistically significant anomaly induced by reducing mineral tracers.

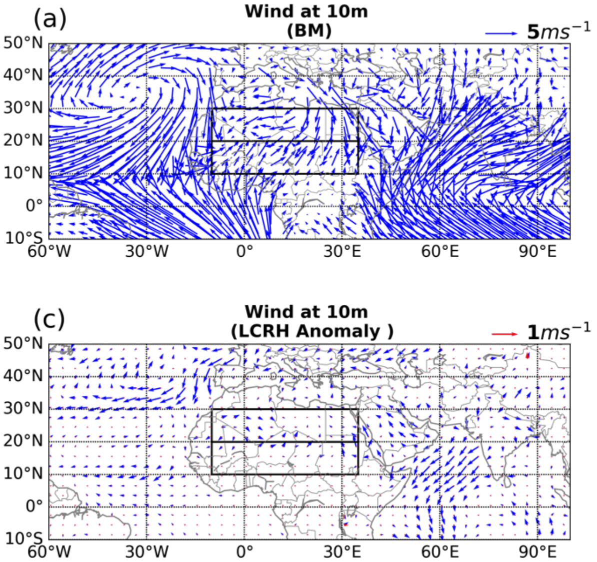

Figure S17. Surface wind at 10m from the reference experiment BM (a) and their anomalies (b), (c) and (d) resulting from reducing mineral tracers in BM-LC, BM-LCRH, and BM-LCRHRG experiment. Statistically significant wind anomalies are highlighted by red arrows.

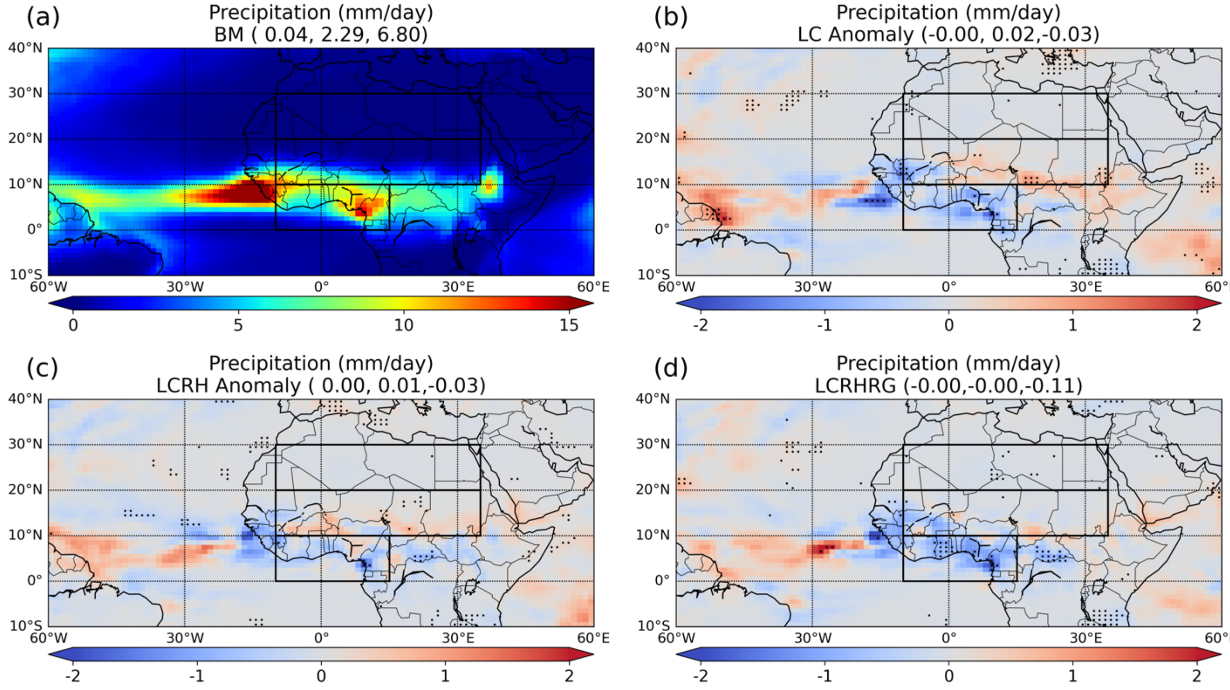

Figure S18. 19-year JJA mean precipitation from the reference experiment BM (a) and their anomalies (b), (c) and (d) resulting from reducing mineral tracers in BM-LC, BM-LCRH, and BM-LCRHRG experiment. The three values in parentheses within the title of each figure is domain averaged values for the Sahara, Sahel, and GC regions. The dotted area denotes anomalies that are statistically significant. Note, for anomalies (b, c, and d), we only average the dotted area, in other words, we only calculate the domain average of statistically significant anomalies.

References:

Gonçalves Ageitos, M., Obiso, V., Miller, R. L., Jorba, O., Klose, M., Dawson, M., Balkanski, Y., Perlwitz, J., Basart, S., Di Tomaso, E., Escribano, J., MacChia, F., Montané, G., Mahowald, N. M., Green, R. O., Thompson, D. R., and Pérez García-Pando, C.: Modeling dust mineralogical composition: sensitivity to soil mineralogy atlases and their expected climate impacts, Atmos. Chem. Phys., 23, 8623–8657, https://doi.org/10.5194/acp-23-8623-2023, 2023.

Prospero, J. M., Ginoux, P., Torres, O., Nicholson, S. E., and Gill, T. E.: Environmental characterization of global sources of atmospheric soil dust identified with the Nimbus 7 Total Ozone Mapping Spectrometer (TOMS) absorbing aerosol product, Rev. Geophys., 40, 2-1-2–31, https://doi.org/10.1029/2000RG000095, 2002.

Ryder, C. L., Marenco, F., Brooke, J. K., Estelles, V., Cotton, R., Formenti, P., McQuaid, J. B., Price, H. C., Liu, D., Ausset, P., Rosenberg, P. D., Taylor, J. W., Choularton, T., Bower, K., Coe, H., Gallagher, M., Crosier, J., Lloyd, G., Highwood, E. J., and Murray, B. J.: Coarse-mode mineral dust size distributions, composition and optical properties from AER-D aircraft measurements over the tropical eastern Atlantic, Atmos. Chem. Phys., 18, 17225–17257, https://doi.org/10.5194/acp-18-17225-2018, 2018.